Available online at www.sciencedirect.com
ScienceDirect
Journal of Magnetic Resonance 188 (2007) 83–96
JMR Journal of Magnetic Resonance
www.elsevier.com/locate/jmr

Random-walk technique for simulating NMR measurements and 2D NMR maps of porous media with relaxing and permeable boundaries

Emmanuel Toumelin [a,1], Carlos Torres-Verdín [a,*], Boqin Sun [b], Keh-Jim Dunn [b]

[a] Department of Petroleum and Geosystems Engineering, The University of Texas, Austin, TX 78712, USA
[b] Chevron Energy Technology Company, San Ramon, CA 94583, USA

Received 18 July 2006; revised 23 May 2007
Available online 17 June 2007

Abstract

We revisit random-walk methods to simulate the NMR response of fluids in porous media. Simulations reproduce the effects of diffusion within external inhomogeneous background magnetic fields, imperfect and finite-duration $\mathbf{B}_1$ pulses, T_1/T_2 contrasts, and relaxing or permeable boundaries. The simulation approach consolidates existing NMR numerical methods used in biology and engineering into a single formulation that expands on the magnetic-dipole equivalent of spin packets. When fluids exhibit low T_1/T_2 contrasts and when CPMG pulse sequences are used to acquire NMR measurements, we verify that classical NMR numerical models that neglect T_1 effects accurately reproduce surface magnetization decays of saturated granular porous media regardless of the diffusion/relaxation regime. Currently, analytical expressions exist only for the case of arbitrary pore shapes within the fast-diffusion limit. However, when fluids include several components or when magnetic fields are strongly inhomogeneous, we show that simulations results obtained using the complete set of Bloch's equations differ substantially from those of classical NMR models. In addition, our random-walk formulation accurately reproduces magnetization echoes stemming from coherent-pathway calculations. We show that the random-walk approach is especially suited to generate parametric multi-dimensional $T_1/T_2/D$ NMR maps to improve the characterization of pore structures and saturating fluids.

Keywords: Random walks; NMR relaxation; Porous media; Fluid typing; 2D NMR

1. Introduction

The application of NMR measurements for pore size characterization of porous and permeable media is motivated by two relationships between measurable quantities and the pore surface-to-volume ratio S/V of porous media saturated with a single fluid phase. First, longitudinal and transversal relaxation times of a fluid (T_1 and T_2, respectively) are related to the product $\rho(S/V)$, where ρ is the relaxivity of the pore surface. This relationship remains valid in the fast-diffusion limit [1] when paramagnetic centers are present at the pore wall surface. Second, the short-time asymptotic behavior of the effective fluid diffusivity D is directly related to S/V [2,3]. Practical limitations exist when applying these two relationships to the interpretation of NMR measurements of porous media. Specifically, it is normally assumed that (1) pores are well defined and isolated, and (2) inversion techniques can reliably and accurately estimate the distribution of surface-to-volume ratios. Experimental evidence shows that pores spanning different length scales can be connected and, therefore, that the estimated values of S/V could be interpreted in an average sense in the presence of low surface relaxivity, such as in certain carbonate rocks [4]. In addition, effective pore values of S/V sensed by protons in a fluid phase depend

* Corresponding author. Fax: +1 512 471 4900.
E-mail address: cverdin@mail.utexas.edu (C. Torres-Verdín).
[1] Present address: Chevron North America Exploration and Production, Houston, TX 77099, USA.

1090-7807/$ - see front matter © 2007 Elsevier Inc. All rights reserved.
doi:10.1016/j.jmr.2007.05.024

on the relative saturation of that phase within the pore: when several fluid phases are present in the same pore space, such as in the case of mixed-wettabilities, the actual and effective values of S/V for that pore may differ substantially. Models used in biological applications to study the influence of membrane permeability on NMR signals also over-simplify the pore structure of biological systems because of the lack of efficient numerical simulation techniques [5–8].

Recently, special acquisition techniques have been developed to improve the accuracy of NMR measurements to assess fluid types [9–11] using (a) suites of magnetic pulse sequences of different magnitudes, orientations, and characteristic times, e.g., CPMG-like sequences with different echo times and wait times, and (b) multi-dimensional inversion of the measured magnetization decays in the form of intensity maps in T_1, T_2, and D domains. Despite these efforts, ambiguities remain when the saturating fluids exhibit similar characteristics, such as light oil and water in water-wet and mixed-wet rocks, because the inversion process is sensitive to fluid diffusivity contrasts, restricted diffusion, surface relaxation, and wettability of the porous medium.

Modern NMR applications require simulation and interpretation methods that can incorporate the complexity of real porous media and multiphase fluid saturation at the pore scale. Accurate simulation methods have been proposed based on coherent pathways for bulk fluids [12–15], or based on analytical diffusion propagators for the case of periodic porous microstructures [16]. However, the disordered nature of most biological and mineral porous media demands more sophisticated approaches for numerical simulation.

The objective of this paper is to develop an accurate an efficient algorithm for the simulation of NMR measurements of saturated microporous media. Specifically, the algorithm is designed to account for known distributions of (a) pore boundaries and surface characteristics (i.e., geometry and surface relaxation ρ and/or diffusion permeability P), (b) static and susceptibility-induced magnetic fields, (c) fluid phases and their bulk properties, and (d) corresponding velocity fields superimposed to the diffusive Brownian motion in the case of ionic displacement [17] or hydraulic motion [18]. After motivating the need for a microscopic description of the pore space to construct quantitative NMR numerical models, we develop the algorithm for the solution of Bloch's equations along the continuous diffusion pathways of random walkers. This approach remains valid when the magnetization coupling between spins in a fluid is governed by constant longitudinal and transversal bulk relaxations, and when Bloch's equations remain valid to describe spin magnetization, i.e., both in the low-field NMR measurement of spin 1/2, and in the high-field ^{1}H measurements of water. Our approach is benchmarked against analytical solutions for complex diffusion/relaxation problems. We then generalize the application of the algorithm for simulating the NMR response of fluids in porous media, and emphasize its key role in parametric multi-dimensional NMR modeling using pore-scale arguments.

2. Macroscopic theory

Macroscopic descriptions of NMR measurements usually invoke three independent processes to describe the relaxation time of the measured magnetization: (1) bulk fluid relaxation, with characteristic longitudinal and transversal times T_{1B} and T_{2B}, mainly due to dipole–dipole interactions between spins within the fluid; (2) surface relaxation, characterized by effective relaxation times T_{1S} and T_{2S}, which occurs because of the proximity with paramagnetic centers at interfaces between pore fluids and grain solids; and (3) relaxation due to the presence of background magnetic field heterogeneities, T_{2D}. The longitudinal and transversal relaxation times measured for a fluid-saturated sample are equal to the harmonic averages [19]

$$\frac{1}{T_1} = \frac{1}{T_{1B}} + \frac{1}{T_{1S}}, \tag{1}$$

and

$$\frac{1}{T_2} = \frac{1}{T_{2B}} + \frac{1}{T_{2S}} + \frac{1}{T_{2D}}. \tag{2}$$

Bulk and surface relaxation times are intrinsic properties given by fluid, porous medium, and thermodynamic state. Bulk relaxations are usually expressed in the form [20,21]

$$T_{1B,2B} = a\frac{T}{\eta} = f(P,T)D_B, \tag{3}$$

where a is a fluid-specific constant, f a thermodynamic function, and P, T, η, and D_B the pressure, temperature, viscosity, and bulk diffusivity of the fluid, respectively. When diffusion–relaxation is controlled by diffusion, i.e., in the fast-diffusion limit $\rho R/D_B < 1$ (R being the pore radius), the surface decay times T_{1S} and T_{2S} are proportional to S/V [1]

$$\frac{1}{T_{1S,2S}} = \rho_{1,2}\frac{S}{V}. \tag{4}$$

The variable T_{2D}, on the other hand, is an experimentally controllable quantity affected by fluid diffusivity, internal fields induced by porous medium magnetic heterogeneities, and instrument configuration. For instance, using a CPMG sequence with constant echo time TE and an applied magnetic gradient G, we have

$$\frac{1}{T_{2D}} = \frac{(\gamma\ G\ \mathrm{TE})^2 D}{12}, \tag{5}$$

where γ is the hydrogen gyromagnetic ratio and D remains the effective diffusivity of the fluid under consideration.

The intrinsic bulk and surface relaxation times affect the time-space evolution of the macroscopic magnetization $\mathbf{M} = (M_x, M_y, M_z)^T$ of a given volume of fluid. Following

Bloch–Torrey's equation in the rotating frame $\Sigma = (\hat{\mathbf{x}}', \hat{\mathbf{y}}', \hat{\mathbf{z}})$, one has [22]:

$$\frac{d\mathbf{M}}{dt} = D_B \nabla^2 \mathbf{M} + \gamma \mathbf{B} \times \mathbf{M} - \frac{M_x}{T_2}\hat{\mathbf{x}}' - \frac{M_y}{T_2}\hat{\mathbf{y}}' - \frac{M_z}{T_1}\hat{\mathbf{z}} + \frac{\mathbf{M}_0}{T_1}. \quad (6)$$

In this equation, $\mathbf{M}_0 = M_0\hat{\mathbf{z}}$ is the equilibrium magnetization aligned with the background magnetic field $\mathbf{B}_0$, and $\mathbf{B} = (B_x, B_y, B_z)^T$ is the total magnetic field that affects the spins in Σ. The magnetic field $\mathbf{B}$ varies as a function of time and space because of (a) inhomogeneous tool background field maps such as described in Fig. 1, (b) susceptibility contrasts between fluid and porous matrix which distort the background field map [16,23], and (c) additional background field gradients used to enhance the NMR decay due to diffusivity contrasts between fluids in low-field applications, or to encode the spin position in high-field MRI applications. When a RF pulse sequence is used to enforce spin refocusing and echo forming, $\mathbf{B}_1$ magnetic pulses superimpose to $\mathbf{B}_0$ for finite durations t_θ. This duration quantifies the amount of magnetization tilting ($\theta = \gamma\|\mathbf{B}_1\|t_\theta$)

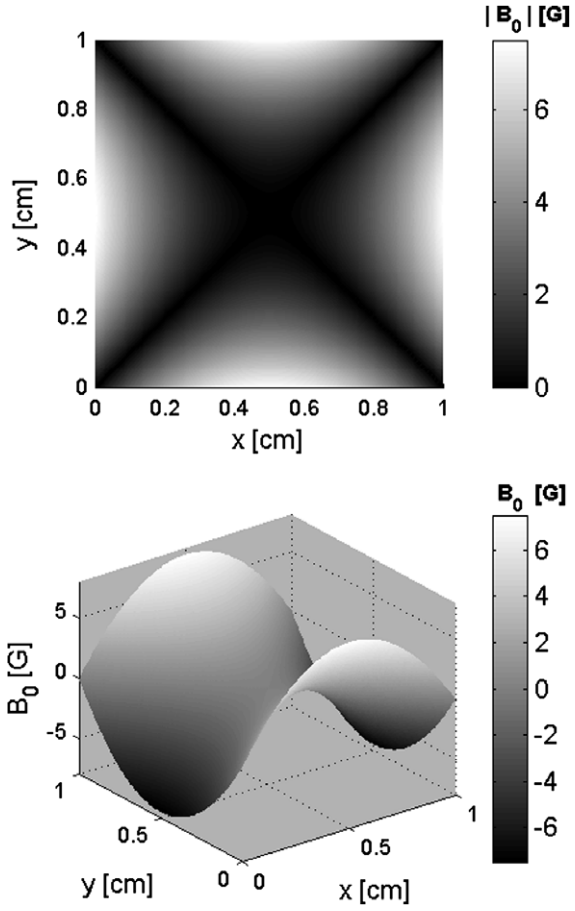

Fig. 1. Magnetic field map representing an approximation of the background magnetic field imposed by the measurement system and adapted from Ref. [12], assuming $\mathbf{B}_0$ of the elliptical form $\mathbf{B}_0 = (-(x/c - 0.5)^2 + (y/c - 0.5)^2 \times 30\ \hat{\mathbf{z}}$ [Gauss], where $c = 1$ cm.

they create through the curl term in Eq. (6)—usually $\pi/2$ or π for the entire pulse duration. For instance, regular CPMG pulse sequences take the form of a $\pi/2$-pulse of duration t_{90} along the $\hat{\mathbf{x}}'$ axis, followed by a series of π pulses of duration t_{180} along the $\hat{\mathbf{y}}'$ axis separated by the inter-echo time $TE = 2\tau$. Spin echoes are stimulated between two successive π pulses. Together with the proximity of relaxing surfaces which affect the relaxation of the spin packets captured by Eq. (6), this variation of $\mathbf{B}$ with both time and space supports a microscopic description wherein such constraints can be explicitly enforced in the numerical formulation.

3. Microscopic random-walk resolution

Random walkers reproducing the diffusive motion of spins have proved to be a reliable and flexible approach to simulate the NMR responses in a variety of porous medium geometries, including fractal or 3D disordered granular porous media [24,25]. In addition, diffusion random walks readily lend themselves to distributed computer environments, thereby considerably reducing computation time. Such algorithms simulate the projection of spin packets in the transversal plane of the rotating frame, i.e., in the plane of measurement of an NMR tool antenna, and describe either surface relaxation effects [4,26] or diffusion effects [23,27]. In this section, we introduce a unified formulation for the simulation of NMR measurements acquired for a wide range of engineering and biological applications.

3.1. Diffusion of equivalent magnetic dipoles

We use a classical continuous random walk, whereby an equivalent magnetic dipole is displaced within the pore space attributed to a given fluid of self-diffusion D_B and bulk relaxation times T_{1B} and T_{2B}. Following an initial location randomly determined within that fluid volume, at each time step of infinitesimal-duration δt a vector of normally distributed random numbers $\mathbf{n} = (n_x, n_y, n_z)$ is generated with unit variance and zero mean. The walker is then spatially displaced in the Cartesian geometrical reference by a vector

$$\delta\mathbf{r}_D = (6D_B\ \delta t)^{1/2}\ \mathbf{n}/\|\mathbf{n}\|. \quad (7)$$

In the presence of velocity drift $\mathbf{v}$ applied to the molecule, an additional drift displacement $\delta\mathbf{r}_V = \mathbf{v}\delta t$ is added to $\delta\mathbf{r}_D$. In so doing, δt is dynamically adapted along the walk so that (a) it is smaller than any magnetic field pulse duration, (b) the amplitude of the total displacement, $\|\delta\mathbf{r} = \delta\mathbf{r}_D + \delta\mathbf{r}_V\|$, is several times smaller than surrounding geometric length scales (e.g., pore throats restricting pore-to-pore connections, wetting film thickness, etc.), (c) the value of the total magnetic field resulting from $\mathbf{B}_0$ and $\mathbf{B}_1$ in the rotating frame can be assumed constant during each step, and (d) all walkers

are synchronized at the onset and offset of magnetic pulses as well as at the time of echo acquisition.

3.2. Magnetization formulation A

We use diffusing random walkers to simulate NMR signals under the assumption that each walker carries a magnetic-dipole equivalent to that of a hydrogen spin packet. Eq. (6) is adapted along each one-dimensional segment by neglecting its convection term in ∇^2 and by defining the evolution matrix $\mathbf{A}$ given by

$$\mathbf{A} = \begin{bmatrix} -\frac{1}{T_2} & \gamma B_z & -\gamma B_y \\ -\gamma B_z & -\frac{1}{T_2} & \gamma B_x \\ \gamma B_y & -\gamma B_x & -\frac{1}{T_1} \end{bmatrix}, \tag{8}$$

and the reduced magnetization

$$\mathbf{M}' = \mathbf{M} + \mathbf{A}^{-1} \cdot \mathbf{M}_0 / T_1. \tag{9}$$

Eq. (6) is integrated as

$$\mathbf{M}'(t) = \mathrm{e}^{\mathbf{A}t} \cdot \mathbf{M}'(0), \tag{10}$$

where $\mathbf{M}'(0)$ is the reduced magnetization at the onset of each integration interval. New appropriate values for B_x, B_y, and B_z are used on each random-walk segment. The relaxation times T_1 and T_2 are also locally adjusted to account for the proximity of a relaxing boundary. Consequently, for each step i spanning the time interval $[t_i, t_i + \delta t_i]$, the spin carried by the random walker is subject to a new evolution matrix $\mathbf{A}^i$ and longitudinal relaxation time T_1^i. This calculation yields the magnetization formulation A

$$\mathbf{M}^i = \mathrm{e}^{(\mathbf{A}^i)\delta t_i} \cdot \left\{ \mathbf{M}^{i-1} + \left(\mathbf{A}^i\right)^{-1} \cdot \frac{\mathbf{M}_0}{T_1^i} \right\} - \left(\mathbf{A}^i\right)^{-1} \cdot \frac{\mathbf{M}_0}{T_1^i}. \tag{11}$$

The total NMR signal is the sum of all $\mathbf{M}$ vectors for all diffusing magnetic dipoles, sampled at the same rate. Hydrogen indices weigh the magnetization contribution of each walker in the presence of multiple fluid phases with different hydrogen index. The Appendix provides analytical solutions for the exponential of matrix $\mathbf{A}$. Tracking the projections of that total magnetization $\mathbf{M}$ onto $\hat{\mathbf{z}}$ and $\hat{\mathbf{y}}'$ with time yields the magnetization polarizations and decays illustrated in Fig. 2. This figure shows the responses of both bulk water and water within relaxing porous medium, simulated with CPMG pulse sequences and different values of wait times (TW) and echo time (TE). Fig. 3 illustrates the joint influence of sampling and step size of the random walks on the accuracy of the simulation results.

3.3. Magnetization formulation B

Previously developed NMR simulation algorithms focused exclusively on reproducing surface relaxation or diffusion within inhomogeneous fields. The latter effect was usually treated in a manner similar to the one described above, except that Bloch's equation was solved

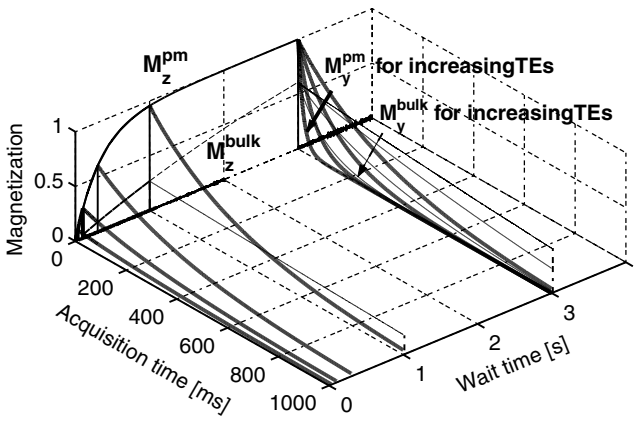

Fig. 2. Amplitude of the mean M_z and M_y magnetizations simulated for 1-s CPMG pulse acquisitions taking place after different wait times for the same volume of bulk water (dashed curves, noted^{bulk}) and water relaxing in the porous medium (continuous curves, noted^{pm}) formed by the void fraction of the disordered grain packing shown in Fig. 10. Surface relaxivity ($\rho_1 = \rho_2 = 20$ μm/s) and pore size (30 μm) were considered uniform. Each magnetic dipole is initially depolarized ($M_z = 0$ and M_y randomly distributed with zero mean), then M_z increases freely for a wait time TW (no RF pulse). Dipoles collectively generate an exponential build-up of the form $1 - \exp(-t/T_1)$. The CPMG RF pulse sequence is then turned on, M_z is tilted by the first $(\pi/2)_x$-pulse into M_y which becomes non-zero and subsequently decays. Next, dipoles collectively generate a macroscopic magnetization in the exponential form $\exp(-t/T_2)$ following the subsequent $(\pi)_y$ refocusing pulses. The results plotted above were simulated for TE = 0.3 ms at TW = 0.03, 0.1, 0.3, and 1 s, and for TE = 0.3, 1, 4, and 16 ms at TW = 3 s.

in the $(\hat{\mathbf{x}}', \hat{\mathbf{y}}')$ projection of Σ by substituting $\mathbf{M}$ in Eq. (6) with a complex magnetization $M^* = M_x + \mathrm{i}M_y$ [28]. In turn, the magnetization was calculated numerically using finite-difference methods [29] or without including a convection term along random-walk trajectories [23,27]. That approach neglected surface as well as longitudinal relaxation effects. Likewise, RF pulses were not accurately reproduced, and $(\pi)_y$ pulses could only be treated as a sign change in the phase of M^* [23], which made the method exclusively amenable to CPMG sequences. The NMR signal was then considered equal to the sum of the cosine of the spin phase shifts, where the phase shifts were equal to the same rotation angle as in the evolution matrix for 3D calculations (see the Appendix), i.e., $\phi = \gamma B \delta t$. For comparison purposes, we also implemented this simulation method in $(\hat{\mathbf{x}}', \hat{\mathbf{y}}')$ space as formulation B.

3.4. Treatment of local surface relaxation

While the walker remains away from a fluid boundary, the relaxation times T_1 and T_2 that affect the equivalent magnetic dipole of the random walker are equal to the bulk fluid longitudinal and transversal relaxation times, T_{1B} and T_{2B}, respectively. However, once the walker is located within one step of a fluid boundary of surface relaxivities ρ_1 (longitudinal) and ρ_2 (transversal), the magnetization decay is locally enhanced to include this surface relaxation effect at the microscopic level. If the displacement achieved

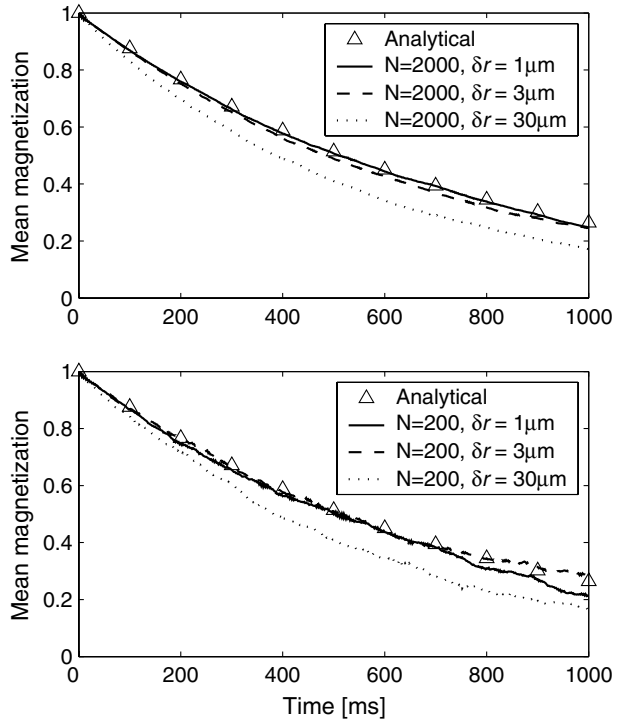

Fig. 3. Influence of walker number (N) and nominal step size (δr) on the accuracy of the numerical simulations. This example simulates the response of a water volume of $2\times2\times2$ mm, with $G = 13.2$ G/cm and TE = 2 ms. The resulting apparent T_2 value is equal to 751 ms. Large values of N are necessary to obtain smooth decays. Even with large N values, too large values of δr create a bias. In this example, no step size larger than 1 μm should be used for maximal accuracy.

during the interval $[t, t+\delta t]$ comes within a distance δr of a fluid boundary, the boundary equation

$$D_{\text{bulk}}\frac{\partial \mathbf{M}}{\partial \hat{\mathbf{n}}} + \begin{bmatrix} \rho_2 & & \\ & \rho_2 & \\ & & \rho_1 \end{bmatrix} \cdot \mathbf{M} = 0 \tag{12}$$

governs the behavior of the relaxation, where the unit vector $\hat{\mathbf{n}}$ describes the normal direction to the surface boundary. For a locally flat boundary, Eq. (12) is solved on a square lattice [30] or for continuous random walks [26] to define a probability of instantaneously 'annihilating' the spin when it reaches the boundary. Bergman et al. [26] solved the boundary condition by integrating diffusion propagators and related that 'annihilating' probability p to surface relaxivity ρ as

$$p = \frac{2}{3}\frac{\rho\delta r}{D_{\text{B}}} \times 0.96. \tag{13}$$

In our model, we consider that each time the walker reaches a relaxing boundary the magnetization decreases by a factor $(1-p)$, or $\exp[-\delta t(p/\delta t)]$ since $p \ll 1$. Therefore, the total relaxation rate becomes $1/T_{1,2} = 1/T_{1\text{B},2\text{B}} + p/\delta t$ for that step. Equivalently, the relaxation times used on each segment of the random walk become

$$\frac{1}{T_{1,2}} = \frac{1}{T_{1\text{B},2\text{B}}} + \varepsilon\frac{3.84\rho_{1,2}}{\delta r}, \tag{14}$$

where $\varepsilon = 1$ when the walker is located within a step of the relaxing boundary, and 0 otherwise.

3.5. Transfer probability of permeable membranes

The case of permeable barriers between pore volumes can be approached in a similar fashion to the case of relaxing surfaces. A boundary exchange rate k_j is defined as the proportionality factor between diffusion flux and concentration difference across a boundary j, in units of time^{-1}. If bulk and surface relaxations can be neglected, then the macroscopic magnetization balance of a compartment bounded by permeable membranes is given in [7,8]

$$\frac{\partial \mathbf{M}}{\partial t} = D_{\text{B}}\nabla^2\mathbf{M} + \gamma\mathbf{B}\times\mathbf{M} - \sum_{\text{outwards}} k_j\mathbf{M} + \sum_{\text{inwards}} k_j\mathbf{M}^{(j)}, \tag{15}$$

where $\mathbf{M}^{(j)}$ is the magnetization within a neighboring compartment j. The sum $\sum$ over outward boundaries acts as a surface sink term whereas the one over inward boundaries acts as a surface source term. Since the surface sink term in Eq. (12) acts as the relaxation decay terms in Eq. (1), the following equivalence holds:

$$\frac{1}{T_2} \equiv \sum_{\text{outwards}} k_j. \tag{16}$$

Furthermore, in the fast-diffusion limit we have $1/T_{2\text{S}} = \rho(S/V)$ [1]; similarly, $k_j = P_j(S/V)$ [7], where P_j is the membrane permeability in units of length per unit time. It is then possible to solve for surface permeability using Bergman et al.'s treatment of surface relaxation: when the walker comes within one step of distance δr from a permeable boundary k, there is a probability of transfer equal to

$$g_k = \frac{2}{3}\frac{P_k\delta r}{D_{\text{B}}} \times 0.96 \tag{17}$$

that the walker crosses the boundary; if that probability is not honored, then the walker bounces back into its original compartment while the clock time is incremented by δt. It is particularly remarkable that both fluid/rock surface relaxation [31] and biological membrane permeability [7] exhibit the same range of values between 0.5 and 30 μm/s. This similarity suggests that the parallel treatment of relaxing or permeable boundaries remains valid on the same range of fluid types and pore sizes.

4. Simulation results in bulk fluid

4.1. Echo sampling

The accuracy of our algorithm is first tested for the case of a homogeneous background magnetic field

gradient. Fig. 4 shows the shapes of the 1st, 2nd, 5th, and 15th CPMG echoes simulated with the random-walk algorithm for different echo times. The results are in excellent agreement with both the measurements and the coherent-pathway calculations of Hürlimann in Ref. [13]. We can therefore conclude that random-walk simulations are a viable and easily implemented alternative to the more complex coherent-pathway calculations.

Hürlimann and Griffin [12] quantified the relative amplitude variation of the stimulated echo (produced by the energy stored during the initial $(\pi/2)_{x'}$-pulse) and of the first spin echo (refocused by the first CPMG $(\pi)_{y'}$ pulses) with coherent-pathway calculations for given field maps and pulse durations. In Fig. 5 we show that similar results are obtained with the random-walk technique. The differences between the results of Ref. [12] and our simulations can be attributed to differences in field map details and

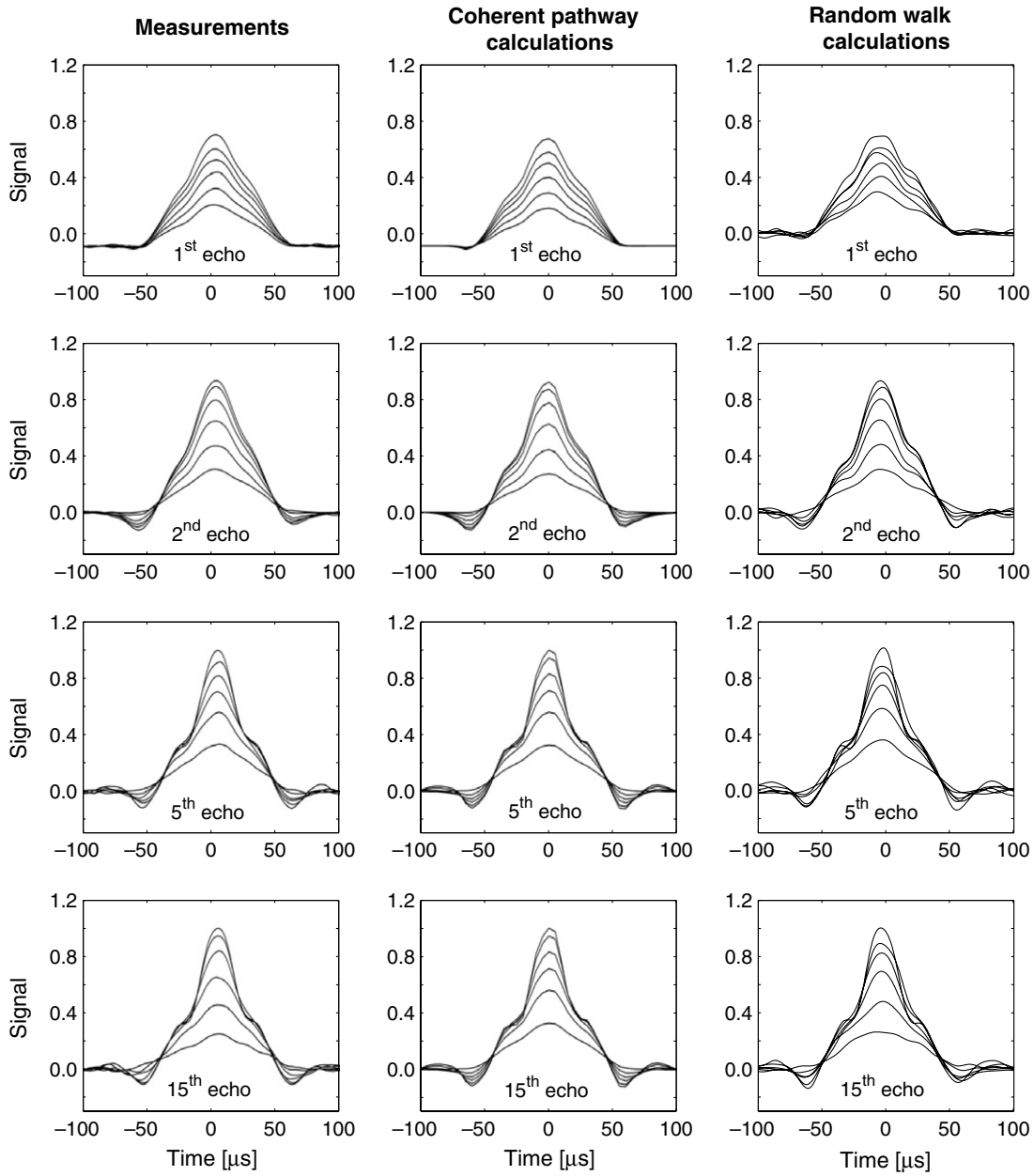

Fig. 4. Comparison between measurements and coherent-pathway calculations from Hürlimann [13], and random-walk simulations of the 1st, 2nd, 5th, and 15th echoes obtained for a CPMG sequence with a water sample. The random-walk simulations considered 20,000 walkers distributed in a volume of $2 \times 2 \times 2$ cm. All results use the same parameters: homogeneous gradient of strength $G = 13.2$ G/cm; pulse durations $t_{180} = 50$ μs, $t_{90} = 25$ μs; for the 1st echo, TE = 0.4, 8.35, 10.35, 12.35, 14.35, and 16.35 ms; for the 2nd echo, TE = 0.4, 4.35, 6.35, 8.35, 10.35, and 12.35 ms; for the 5th echo, TE = 0.4, 2.35, 3.75, 4.95, 6.35, and 8.35 ms; for the 15th echo, TE = 0.4, 1.354, 2.75, 3.75, 4.95, and 6.35 ms. The time scale is centered with the midpoint between the pulses that immediately precede and follow the echoes.

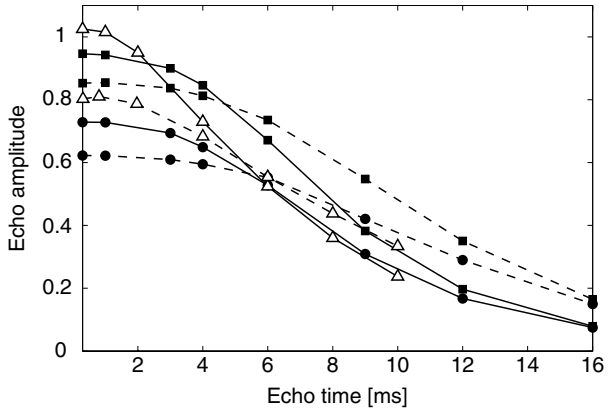

Fig. 5. Amplitudes of the first (dash) and second (plain) CPMG echoes simulated as a function of echo time for 1 cm^3 of bulk water volume. Curves with square and circle markers identify the mean M_y signal simulated with 10,000 random walkers in the field map of Fig. 1, for different $\mathbf{B}_1$ pulse widths (square markers: $t_{90} = 10$ μs, $t_{180} = 15$ μs; circle markers: $t_{90} = 20$ μs, $t_{180} = 30$ μs). Calculations reported in Ref. [12] for a similar field map are plotted with open triangle markers.

homogeneity of the background magnetic field. In all cases, the amplitude of the first echo is remarkably lower than that of the second echo for TE <5 ms, and becomes larger when TE increases.

Dispersion of magnetic field strength—and therefore of Larmor frequencies—throughout the volume enhances the precession decay and the creation of echoes due to the RF π pulses of a CPMG sequence. When the duration of these RF pulses increases, then the measurable echo amplitude decreases. Background field maps can therefore be optimized to maximize the signal obtained during measurement acquisition. These remarks are illustrated in Fig. 6, where the formation of echoes in 1 cm^3 of water is simulated with our random-walk method (formulation A) through spin refocusing between two π pulses, for different pulse widths and two permanent magnetic field maps. As the duration of the RF pulses increases, the quality of the echoes degrades through lower amplitudes and larger spread. In these tests, the field map shown in Fig. 1 generates higher echo amplitudes, hence higher signal, than that of a homogeneous magnetic gradient.

The magnetization decays considered in the following sections of this paper are taken as the envelopes of maximal values reached at each M_y echo.

4.2. Decay in an inhomogeneous background magnetic field

We now compare the decays generated by the presence of background magnetic gradients between (1) random-walk formulation A, (2) random-walk formulation B, and (3) the normalized apparent decay $M = \exp[-t(1/T_{2B} + 1/T_{2D})]$. Because the M_y signal obtained using formulation A is sensitive to large sampling volumes and imperfections in the magnetic field distribution, all its simulated decays were normalized at the time origin. Fig. 7 compares simulation results for two values of homogeneous gradient, $G_z = 12$ and 29 G/cm, three echo times, TE = 0.3, 1, and 3 ms, and two sampling volumes, 1 mm^3 and 1 cm^3. Formulation B yields the same decays regardless of the sample

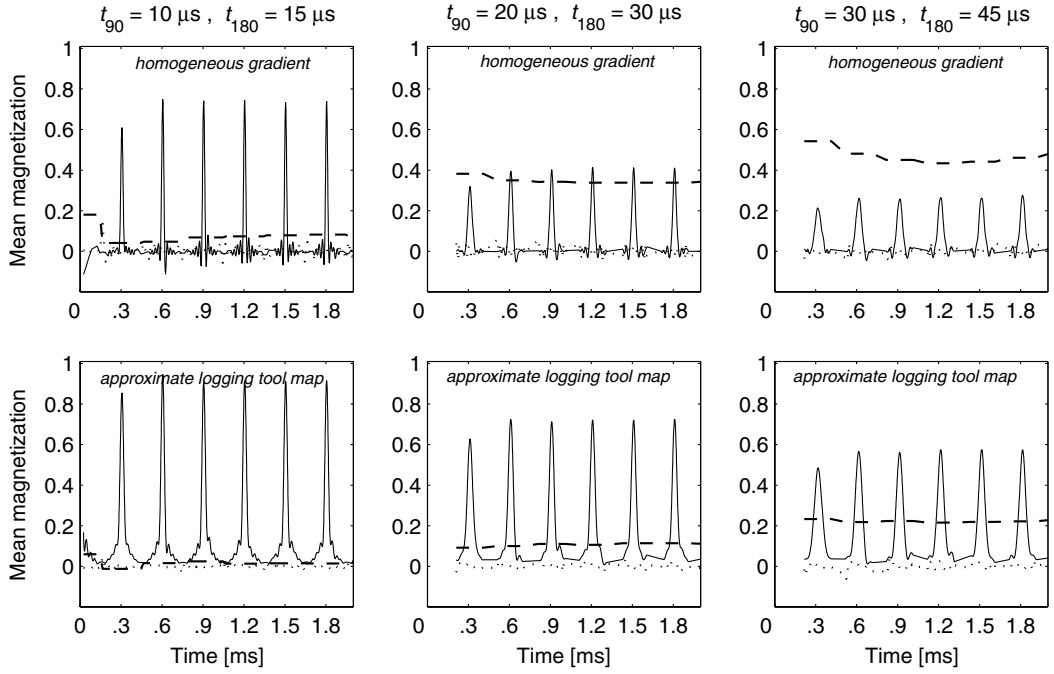

Fig. 6. Impact of background gradient on NMR echo amplitudes. The mean NMR magnetization is calculated from 20,000 walkers for a water volume of 1 cm^3, 300-μs echo time CPMG sequence, and different values of t_{90} and t_{180}. Plain curves identify M_y projection (signal); dotted curves, M_x (out-of-phase noise); dashed curves, M_z. Top row: simulations performed with a homogeneous permanent gradient $G_z = 20$ G/cm. Bottom row: simulations performed with the field map described in Fig. 1.

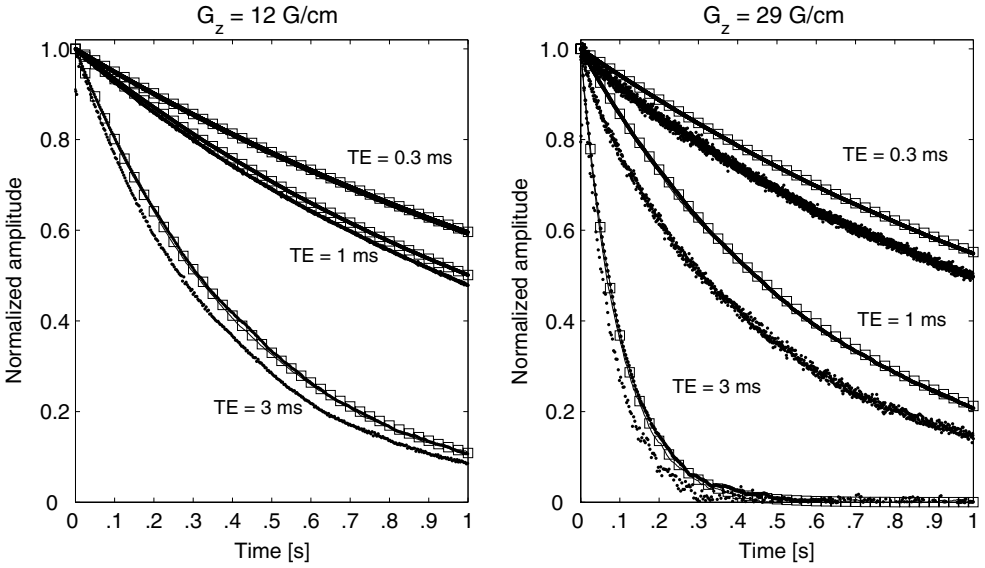

Fig. 7. NMR decay for CPMG pulse acquisition of bulk water in a homogeneous background magnetic gradient G_z for different values of TE and for magnetization formulations A and B. Open square markers describe the analytical solution; simulation results of Formulation A are described by continuous curves for a 1 mm^3 simulated water sample, and by dots for a 1 cm^3 water sample. For each value of TE and each sampling volume, Formulation B yields results that exactly match the analytical solution.

volume and exactly matches the analytical decays. Formulation A also perfectly fits the analytical results for the smaller sampling volume, but exhibits substantial differences for the larger volume. This effect is due to the distribution of the energy acquired during the different RF pulses, as mentioned in Section 4.1, and cannot be accounted for by formulation B or by standard analytical expressions that disregard the finite duration of the RF pulses.

4.3. T_1 scaling

It is customary to consider that the NMR decay obtained for a fluid after partial repolarization of duration TW is equal to the decay at full polarization (i.e., starting from $\mathbf{M} = \mathbf{M}_0$, or $\mathrm{TW} \to \infty$) weighted by the value $(1 - \exp(-\mathrm{TW}/T_1))$. Fig. 8 shows that this treatment is appropriate for a simple-component fluid such as 7-cp oil with unimodal bulk relaxation time at 200-ms in laboratory conditions. For a 300-cp multi-component heavy oil with 40-ms relaxation peak value (distribution shown in the insert of Fig. 8), the decays obtained after partial polarization are normalized so that the amplitude of each decay is 1 when $t = 0$. For a known distribution of bulk relaxations of the multi-component fluid, each walker accounted for a molecule of one miscible component of that fluid, and was stochastically assigned values of bulk relaxation time and diffusivity so that the T_2 distribution was honored over the entire population of random walkers. The normalized decays show that no scaling exists between the different decays due to the wide distribution of relaxation times. In the presence of strong internal fields, the apparent values of T_2 would also span a wide relaxation range, but without

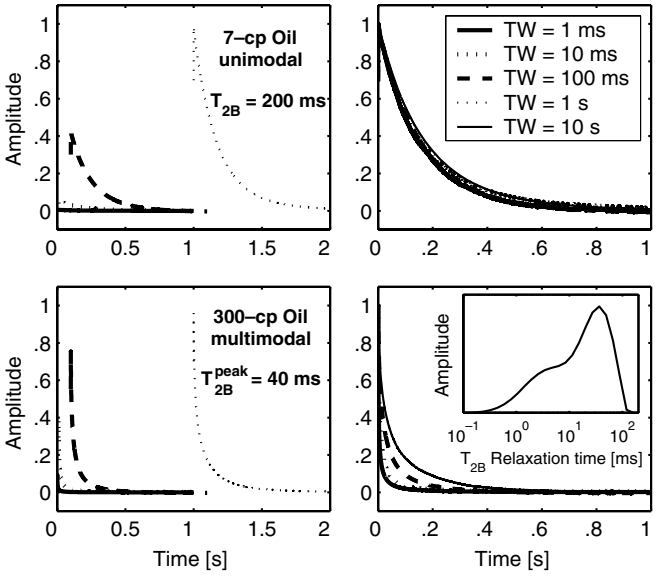

Fig. 8. NMR magnetization decays of bulk fluids simulated for different values of wait time (left panels), and equivalent decays normalized in amplitude at time $t = 0$ (right-hand panels). The same legend applies to all panels. For simple fluids with unimodal distribution of bulk relaxation times (top-right panel), all curves scale with TW and overlap with the canonical form $(1 - \exp(-\mathrm{TW}/T_1)) \times \exp(-t/T_2)$. For multi-component hydrocarbons (bottom right-hand panel), such normalized curves do not overlap. The insert describes the distribution of bulk relaxation times for the 300-cp heavy oil measured at laboratory conditions, and is used as input to the simulation algorithm.

the corresponding spread in the T_1 spectrum. Again, in this case no scaling will exist between the magnetization decays measured after incomplete polarizations with different wait times. Because only Formulation A incorporates T_1 build-up, it needs to be used for the cases of strong

heterogeneities in bulk relaxation and internal fields to ensure accurate simulation results for partial polarization.

5. Simulation results in saturated porous media

We now study how the incorporation of a porous medium exhibiting surface relaxation affects the quality of the simulation results. Different relaxation types are incorporated simultaneously to generate parametric multi-dimensional NMR maps with the purpose of characterizing pore size, wettability, fluid type and volumetric fraction in the context of saturated rock-core analysis and in-situ oil field evaluation.

5.1. Surface relaxation in different diffusion/relaxation regimes

We test our algorithm for the classical context of an isolated spherical pore of radius R, where $S/V = 3/R$. Fig. 9 shows the results of simulations performed with different spherical pore radii ranging from 0.4 to 400 μm, and for different values of surface relaxivity. In all the cases, the simulation decays obtained with both formulations A and B perfectly overlap in the absence of ρ_1/ρ_2 contrast, as encountered in natural systems; for example, it is observed that this contrast usually does not exceed 1.5 in water-saturated rocks [31]. If this contrast were to reach several units, however, differences in apparent decay times would appear between formulations A and B. Likewise, a local increase of the gradient due to diamagnetic or paramagnetic materials in the solid phase of the porous medium is more likely to affect simulation results using formulation A because of the finite duration of the $\mathbf{B}_1$ pulses.

The simulation results shown in Fig. 9 match the first-order surface relaxation time described by Eq. (4) as long as $\rho R/D_B < 1$. Identical results were obtained in the 3D star-shaped pores formed by the void space fraction existing within a dense packing of overlapping spherical grains with different compaction coefficients.

Outside the fast-diffusion limit, that is when $\rho R/D_B$ becomes larger than 1, the surface relaxation described by Eq. (4) becomes inaccurate. It is then necessary to consider Brownstein and Tarr's [1] full analytical solution, whereby the total magnetization decay due to surface relaxation is equal to

$$M(t) = M(0)\sum_{n=0}^{\infty} I_n e^{-t/T_n}. \tag{18}$$

In this expression, $I_n = \frac{12(\sin\zeta_n - \zeta_n\cos\zeta_n)^2}{\zeta_n^3[2\zeta_n - \sin(2\zeta_n)]}$ and $T_n = R^2/D\zeta_n^2$ are the amplitude and relaxation time defined by ζ_n, the nth positive root of the equation

$$1 - \zeta_n \cot\zeta_n = \rho R/D. \tag{19}$$

In Fig. 9, simulation results show the deviation from Eq. (4) to Eq. (18) is correctly captured by the random-walk algorithm for any value of $\rho R/D_B$.

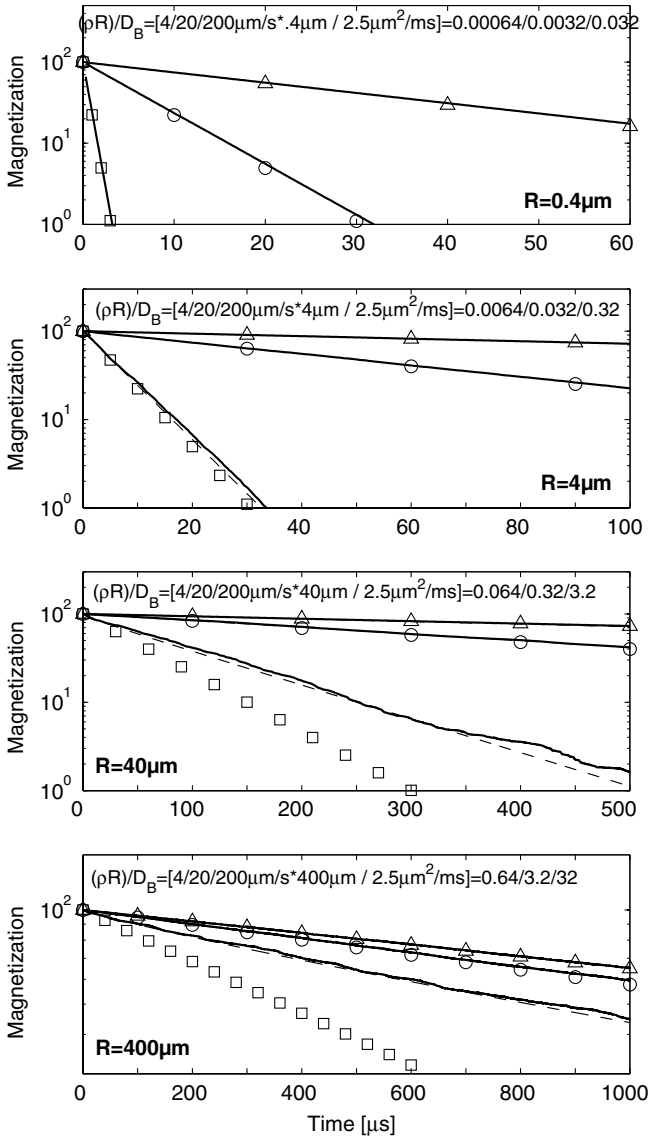

Fig. 9. Decay curves simulated for water ($D_B = 2.5$ μm²/ms, $T_{2B} = 3$ s) in a single spherical pore with no background magnetic field gradient. The pore radius R varies logarithmically from 0.4 (top panel) to 400 μm (bottom panel), while for each radius the surface relaxivity ρ at the pore wall is equal to 4 μm/s (triangles), 20 μm/s (circles) or 200 μm/s (squares). These markers define the first-order analytical decay for a sphere ($1/T_2 = 1/T_{2B} + 3\rho/R$) which diverges from the full expression of Brownstein and Tarr [1] (in dashes) when $\rho R/D_B$ reaches 1, Eq. (18). Results simulated with formulations A and B overlap (plain lines) and almost perfectly match the full analytical expression in all cases. The ratio $\rho R/D_B$ is computed within the panels for each combination of R and ρ.

5.2. Two-dimensional NMR maps of gas/water and oil/water mixtures in saturated rocks

In oil exploration and rock/fluid characterization, fluids measured by in-situ NMR logging tools include brine, single- and multi-component oil, gas, and water-based or oil-based drilling-mud filtrate which leaked into a freshly drilled porous rock formation. Multi-dimensional NMR techniques are currently based on the simultaneous

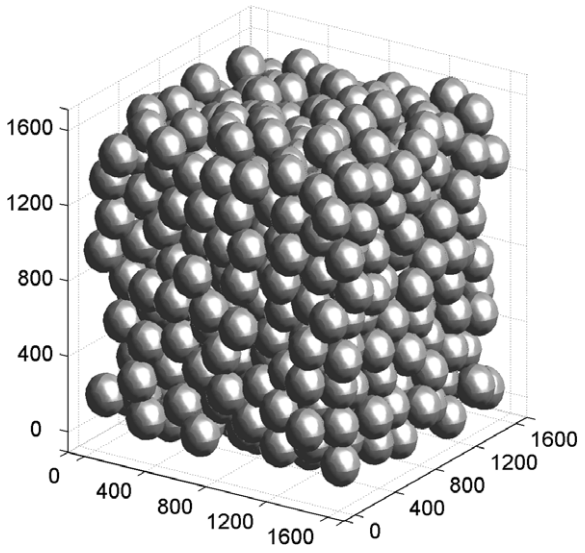

Fig. 10. Example of disordered packing of identical grains used as rock model to generate the 2D NMR maps shown in Figs. 12 and 13. The spherical grains are overgrown until the void fraction reaches 20% of the bulk volume.

inversion of suites of CPMG-like sequences with multiple values of TE and/or TW which allow different degrees of spin repolarization between successive CPMG RF sequences (Fig. 2). Fluid phases are distributed in the pore space of a disordered grain pack (Fig. 10) according to geometrical models in agreement with thermodynamic capillary equilibrium [32] or with more complex principles of drainage, imbibition, and electrical properties [33]. In these models, as exemplified in Fig. 11, fluid phases are distributed at the pore level as overlapping blobs which are truncated by grain surfaces. Two examples of rock/fluid systems were simulated to illustrate the methodology in disordered packs of overlapping spheres exhibiting 20% void space, uniform distribution of pore sizes, and enforcing a homogeneous gradient with $G_z = 16$ G/cm.

The first example was simulated for a mixture of 30% water and 70% gas in arbitrary reservoir conditions, whose bulk properties are shown in Table 1. Wait times varying logarithmically from 1 ms to 10 s were applied during the simulations of CPMG decay with 0.2 ms echo time, and the corresponding magnetization decays were processed with a T_1/T_2 inversion algorithm [11]. The left-hand panel of Fig. 12 shows the resulting intensity T_1/T_2 map, where the water peak located at $T_1 = T_2 = 100$ ms is affected by surface decay. The small echo time has negligible influence on the T_2 response of the low-diffusivity water; however, it significantly reduces the apparent T_2 value of the large-diffusivity gas with respect to its intrinsic T_1 value. In this case, inversion of the T_1 dimension efficiently discriminates the signals from the two fluids. We also synthesized magnetization decays for multiple-TE diffusion sequences for D/T_2 inversion and mapping. This was done by considering full polarization ($TW \to \infty$) and values of TE equal to 0.2, 1, 3, 9, and 16 ms for a homogeneous gradient $G_z = 16$ G/cm. Focusing on the same water/gas mixture saturating our porous rock model, we obtain the D/T_2 map shown in the right-hand panel of Fig. 12. In this plot, as in subsequent D/T_2 maps, the diagonal line characterizes a D/T_2 correlation existing for live hydrocarbons at specific conditions of pressure and temperature (Eq. (3)). In this plot, water and gas are distinguishable on both the D and T_2 dimensions.

Table 1
Bulk properties of the fluids used in the numerical simulation of NMR measurements of saturated rocks

Fluid	Hydrogen index	Bulk relaxation times $T_{1B} = T_{2B}$	Bulk diffusivity D_B (cm^2/s)
Water	1.0	3 s	$2 \cdot 10^{-5}$
Gas	0.3	4.5 s	10^{-3}
7-cp oil	1.0	0.2 ms	10^{-6}

Our second example consists of a mixture of 60% water and 40% 7-cp oil at ambient conditions (see Table 1) within the same rock model, and illustrates the simulation of wettability effects at the rock surface. The same diffusion sequences were implemented, and the simulation results were inverted into the D/T_2 maps shown in Fig. 13. Simulation results for the water-wet case (left-hand panel) exhibit a water peak at the intersection of the bulk water diffusivity (2.10^5 m^2/ms) and the surface relaxation time previously observed in Fig. 13 (100 ms). The oil peak, however, lies along the D/T_2 hydrocarbon correlation line. The (D, T_2) coordinates of that peak along that line enable the assessment of oil viscosity and possibly water-wettability. Upon wettability alteration, it is usually assumed that the water film existing between oil and rock surface ruptures under different chemical and thermodynamic conditions [34,35], while the least attainable zones of the pore space remain water-wet (see Fig. 11). The right-hand panel of Fig. 13 shows simulation results obtained when such microscopic geometries are included in the model. When oil is considered as the wetting fluid phase, it is affected by surface relaxation and the spread of its D/T_2 peak increases along both the D and T_2 dimensions. Concomitantly, the relaxation time of the water peak increases because some relaxing water/rock surfaces have disappeared, and some of the water now relaxes in bulk mode. Because of the low T_{1B}/T_{2B} contrasts for water and oil, the low gradient value, and because of the choice of CPMG acquisition sequence, Formulation B was computationally efficient in this particular case. We emphasize, however, that Formulation A would be required for more general RF sequences or in the presence of stronger magnetic field gradients.

The random-walk algorithm developed in this paper can be used to quantify the impact on NMR measurements of the combined effects of fluid content, fluid viscosity, saturation history of the porous medium, and rock wettability. For instance, Refs. [32,33] study the reliability of D/T_2 2D NMR interpretation to accurately assess hydrocarbon content and rock properties under the assumption of specific fluid displacement mechanisms within the pore space.

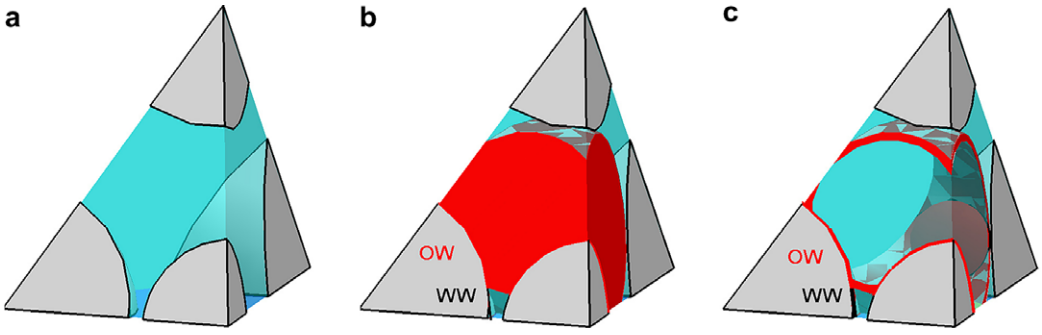

Fig. 11. Examples of fluid distributions implemented at the pore scale. Each tetrahedron is centered on a pore from the void space of the grain packing (Fig. 10), and is limited by sets of four-closest grains (in gray). Blue represents the water-filled pore space, red the oil-filled pore space. (a) Water fills the pore. (b) An oil blob centered with the pore under the double assumption of oil-wettability (OW) of the grain surface within the radius of the oil blob, and water-wettability (WW) of the grain surface in the least-accessible pore regions. (c) A thin film of wetting oil and bridging oil lenses are left in the oil-wet region of the pore after invasion by water. The random-walk step is adjusted within each fluid zone.

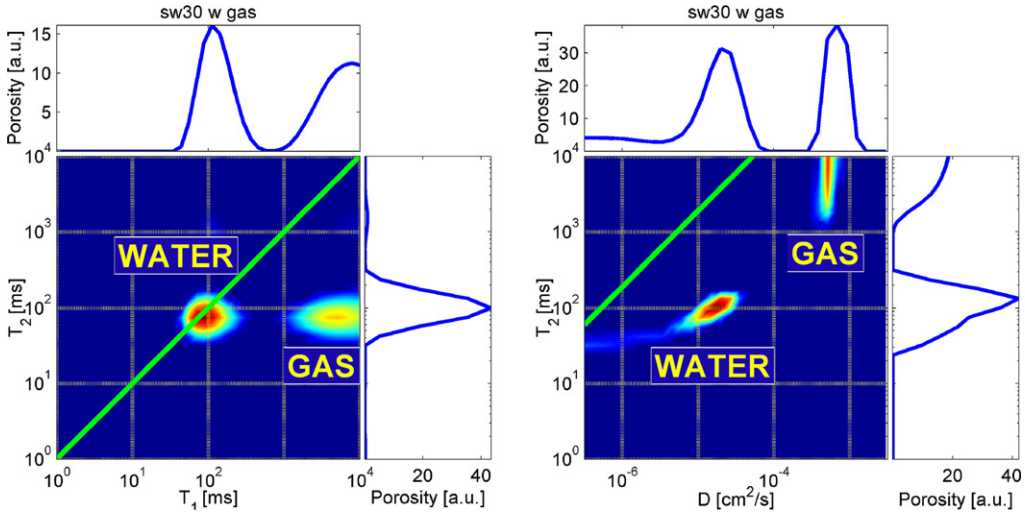

Fig. 12. T_1/T_2 (left) and D/T_2 (right) NMR maps simulated for a two-phase immiscible mixture of 70% gas and 30% water in the grain packing of Fig. 10. The diagonal line in the left-hand panel represents the $T_1 = T_2$ relationship. The diagonal line in the right-hand panel represents the D/T_2 correlation characterizing hydrocarbons in the conditions assumed for the simulations (after Ref. [32]).

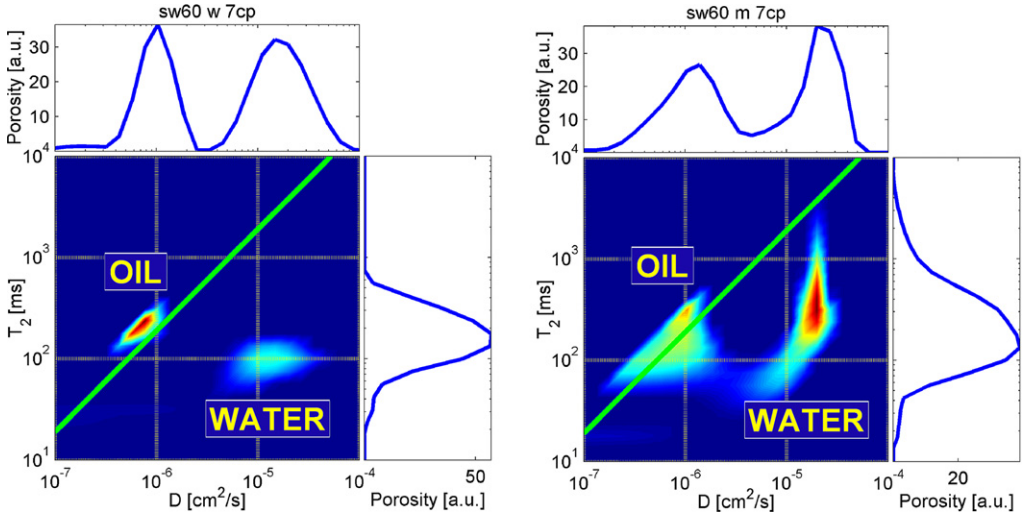

Fig. 13. D/T_2 NMR maps simulated for a two-phase immiscible mixture of 60% water and 40% 7-cp oil in the grain packing of Fig. 10, for water-wet (left-hand panel) and oil-wet (right-hand panel) configurations. The diagonal line in the two panels represents the D/T_2 correlation characterizing hydrocarbons in the conditions assumed for the simulations (after Ref. [32]).

6. Conclusions

The simulation algorithm described in this paper consolidates existing NMR numerical simulation methods used in diverse areas of biology and engineering into a single formulation that incorporates both diffusion within inhomogeneous magnetic fields and surface effects, including magnetization relaxivity and membrane permeability. Other than the magnetic-dipole approximation, this formulation is constrained by none of the assumptions required for analytical models concerning the statistical distribution of spin phase shifts, spin density, field homogeneity, or fast-diffusion limit. In addition, the simulation algorithm described in this paper extends NMR simulation capabilities beyond those of single-phase periodic media, which are so far the only type of porous media that can be accurately described with analytical techniques.

Previously described NMR simulations techniques neglected longitudinal effects; while it is expected that those techniques would not accurately reproduce the NMR response of molecules with substantial T_1/T_2 contrasts, we showed that the solution of the complete set of Bloch's equations is necessary to accurately reproduce echo amplitudes in the presence of strongly inhomogeneous magnetic fields and arbitrary pulse sequences. The simulation algorithm described in this paper was successfully validated against coherent-pathway results in homogeneous gradients and against the full expansion of Brownstein and Tarr's surface relaxation in spherical pores; these results suggest that random walkers can reliably be used to accurately characterize diffusion in arbitrary porous media, where analytical expressions are not accurate.

We considered suites of longitudinal and transversal magnetizations for multiphase fluid mixtures saturating models of porous media for different values of wait time and echo time. These synthetic magnetizations can be subsequently inverted into parametric multi-dimensional intensity maps cross-plotting T_1, T_2, and D for improved characterization of pore structure, wettability, and fluid types. Such a methodology provides new opportunities to study quantitative relationships between NMR measurements and properties of economic interest that cannot be directly measured in-situ [31]. Moreover, the accurate simulation of magnetization decay opens the possibility of optimizing new NMR pulse acquisition sequences for specific applications in porous media in the presence of local variations of fluid distributions and internal fields.

Appendix A. Analytical calculations of the time-evolution matrix exponentials in Bloch's equation

The total magnetic field applied to the spin $\mathbf{B} = \mathbf{B}_0 + \mathbf{B}_1$ is either $\mathbf{B} = \mathbf{B}_0 = B_0\hat{\mathbf{z}}$ between RF pulses, $\mathbf{B} = B_1\hat{\mathbf{x}} + B_0\hat{\mathbf{z}}$ during x'-pulses, or $\mathbf{B} = B_1\hat{\mathbf{y}} + B_0\hat{\mathbf{z}}$ during y'-pulses. This approach makes no approximation on the quality of magnetic pulses because the actual dispersion of Larmor frequencies is honored across the spin population and the spin diffusion is fully accounted for during the enforcement of $\mathbf{B}_1$.

Between $\mathbf{B}_1$ pulses, the only magnetic field present is the background field, and the effective relaxation times $T_{1,2}$ for that step are given by Eq. (14). It then follows that

$$\mathbf{A}\delta t = \begin{bmatrix} -\frac{\delta t}{T_2} & \gamma B_z \delta t & 0 \\ -\gamma B_z \delta t & -\frac{\delta t}{T_2} & 0 \\ 0 & 0 & -\frac{\Delta t}{T_1} \end{bmatrix}, \quad \text{and therefore}$$

$$\mathrm{e}^{\mathbf{A}\delta t} = \begin{bmatrix} \mathrm{e}^{-\frac{\delta t}{T_2}}\cos(\gamma B_z \delta t) & \mathrm{e}^{-\frac{\delta t}{T_2}}\sin(\gamma B_z \delta t) & 0 \\ -\mathrm{e}^{-\frac{\delta t}{T_2}}\sin(\gamma B_z \delta t) & \mathrm{e}^{-\frac{\delta t}{T_2}}\cos(\gamma B_z \delta t) & 0 \\ 0 & 0 & \mathrm{e}^{-\frac{\delta t}{T_1}} \end{bmatrix}. \tag{A1}$$

During $\mathbf{B}_1$ $(\pi/2)_x$ pulses, the product $\mathbf{A}\delta t$ takes on the form

$$\mathbf{A}\delta t = \begin{bmatrix} -\frac{\delta t}{T_2} & \gamma B_z \delta t & 0 \\ -\gamma B_z \delta t & -\frac{\delta t}{T_2} & \gamma B_x \delta t \\ 0 & -\gamma B_x \delta t & -\frac{\delta t}{T_1} \end{bmatrix}. \tag{A2}$$

The three eigenvalues λ_i of $\mathbf{A}\delta t$ are found by solving the characteristic polynomial given by

$$\begin{aligned} P_x(\lambda) &= \det(\lambda\mathbf{I} - \mathbf{A}\delta t) \\ &= \lambda^3 + \lambda^2\left(\frac{2\delta t}{T_2} + \frac{\delta t}{T_1}\right) \\ &\quad + \lambda\left(\frac{2(\delta t)^2}{T_2 T_1} + \frac{(\delta t)^2}{T_2^2} + (\gamma B_x \delta t)^2 + (\gamma B_z \delta t)^2\right) \\ &\quad + \left(\frac{(\delta t)^3}{T_2^2 T_1} + \frac{(\delta t)^3(\gamma B_x)^2}{T_2} + \frac{(\delta t)^3(\gamma B_z)^2}{T_1}\right), \end{aligned}$$

which we solve using Cardan's method

$$\begin{cases} \lambda_1 = \sqrt[3]{(s-q)} - \sqrt[3]{(s+q)} - \frac{a}{3}, \\ \lambda_2 = \frac{1}{2}\left(\sqrt[3]{(s+q)} - \sqrt[3]{(s-q)}\right) - \frac{a}{3} + \frac{\mathrm{i}\sqrt{3}}{2}\left(\sqrt[3]{(s+q)} + \sqrt[3]{(s-q)}\right), \\ \lambda_3 = \frac{1}{2}\left(\sqrt[3]{(s+q)} - \sqrt[3]{(s-q)}\right) - \frac{a}{3} - \frac{\mathrm{i}\sqrt{3}}{2}\left(\sqrt[3]{(s+q)} + \sqrt[3]{(s-q)}\right), \end{cases} \tag{A3}$$

$$\text{with} \quad p = \frac{1}{3}\left(b - \frac{a^2}{3}\right); \quad q = \frac{1}{2}\left(c - \frac{ab}{3} + \frac{2a^3}{27}\right); \quad s = \sqrt{q^2 + p^3}, \quad \text{and}$$

$$a = \left(\frac{2\delta t}{T_2} + \frac{\delta t}{T_1}\right); \quad b = \left(\frac{2(\delta t)^2}{T_2 T_1} + \frac{(\delta t)^2}{T_2^2} + (\gamma B_x \delta t)^2 + (\gamma B_z \delta t)^2\right);$$

$$c = \left(\frac{(\delta t)^3}{T_2^2 T_1} + \frac{(\delta t)^3(\gamma B_x)^2}{T_2} + \frac{(\delta t)^3(\gamma B_z)^2}{T_1}\right). \tag{A4}$$

A matrix of eigenvectors corresponding to the above eigenvalues can be calculated as

$$\mathbf{U} = \begin{bmatrix} \frac{\gamma B_z \delta t}{\lambda_1 + \frac{\delta t}{T_2}} & \frac{\gamma B_z \delta t}{\lambda_2 + \frac{\delta t}{T_2}} & \frac{\gamma B_z \delta t}{\lambda_3 + \frac{\delta t}{T_2}} \\ 1 & 1 & 1 \\ -\frac{\gamma B_x \delta t}{\lambda_1 + \frac{\delta t}{T_1}} & -\frac{\gamma B_x \delta t}{\lambda_2 + \frac{\delta t}{T_1}} & -\frac{\gamma B_x \delta t}{\lambda_3 + \frac{\delta t}{T_1}} \end{bmatrix},$$

whereupon,

$$e^{\mathbf{A}\delta t} = \mathbf{U} \cdot \begin{bmatrix} e^{\lambda_1} & 0 & 0 \\ 0 & e^{\lambda_2} & 0 \\ 0 & 0 & e^{\lambda_3} \end{bmatrix} \cdot \mathbf{U}^{-1}.$$

During $\mathbf{B}_1$ $(\pi)_y$ pulses, $\mathbf{A}\delta t$ takes on the form

$$\mathbf{A}\delta t = \begin{bmatrix} -\frac{\delta t}{T_2} & \gamma B_z \delta t & -\gamma B_y \delta t \\ -\gamma B_z \delta t & -\frac{\delta t}{T_2} & 0 \\ \gamma B_y \delta t & 0 & -\frac{\delta t}{T_1} \end{bmatrix}.$$

Upon replacing B_x with B_y in Eq. (A4), it is readily found that the eigenvalues of this last matrix are identical to those of Eq. (A3). The corresponding eigenvectors are included in matrix $\mathbf{U}$ as

$$\mathbf{U} = \begin{bmatrix} 1 & 1 & 1 \\ -\frac{\gamma B_z \delta t}{\lambda_1 + \frac{\delta t}{T_2}} & -\frac{\gamma B_z \delta t}{\lambda_2 + \frac{\delta t}{T_2}} & -\frac{\gamma B_z \delta t}{\lambda_3 + \frac{\delta t}{T_2}} \\ \frac{\gamma B_y \delta t}{\lambda_1 + \frac{\delta t}{T_1}} & \frac{\gamma B_y \delta t}{\lambda_2 + \frac{\delta t}{T_1}} & \frac{\gamma B_y \delta t}{\lambda_3 + \frac{\delta t}{T_1}} \end{bmatrix}.$$

The computation of $e^{\mathbf{A}\delta t}$ follows directly from the above expressions.

References

[1] K.R. Brownstein, C.E. Tarr, Importance of classical diffusion in NMR studies of water in biological cells, Phys. Rev. A 19 (1979) 2446–2453.

[2] L.L. Latour, P.P. Mitra, R.L. Kleinberg, C.H. Sotak, Time-dependent diffusion coefficient of fluids in porous media as a probe of surface-to-volume ratio, J. Magn. Res. A 101 (1993) 342–346.

[3] Y.-Q. Song, Determining pore sizes using an internal magnetic field, J. Magn. Res. 143 (2000) 397–401.

[4] T.S. Ramakrishnan, L.M. Schwartz, E.J. Fordham, W.E. Kenyon, D.J. Wilkinson, Forward models for nuclear magnetic resonance in carbonate rocks, Log Analyst 40 (1999) 260–270.

[5] E. von Meerwall, R.D. Ferguson, Interpreting pulsed-gradient spin-echo diffusion experiments with permeable membranes, J. Chem. Phys. 74 (1981) 6956–6959.

[6] J. Pfeuffer, W. Dreher, E. Sykova, D. Leibfritz, Water signal attenuation in diffusion-weighted ^{1}H NMR experiments during cerebral ischemia: influence of intracellular restrictions, extracellular tortuosity, and exchange, Magn. Res. Imag. 16 (1998) 1023–1032.

[7] G.J. Stanisz, A. Szafer, G.A. Wright, R.M. Henkelman, An analytical model of restricted diffusion in bovine optic nerve, Magn. Res. Med. 37 (1997) 103–111.

[8] G.P. Zientara, J.H. Freed, Spin-echoes for diffusion in bounded, heterogeneous media: a numerical study, J. Chem. Phys. 72 (1980) 1285–1292.

[9] M.D. Hürlimann, L. Venkataramanan, Quantitative measurement of two-dimensional distribution functions of diffusion and relaxation in grossly inhomogeneous fields, J. Magn. Res. 157 (2002) 31–42.

[10] B. Sun, K.-J. Dunn, Probing the internal field gradients of porous media, Phys. Rev. E 65 (2002) 051309.

[11] B. Sun, K.-J. Dunn, A global inversion method for multi-dimensional NMR logging, J. Magn. Res. 172 (2005) 152–160.

[12] M.D. Hürlimann, D.D. Griffin, Spin dynamics of Carr–Purcell–Meiboom–Gill-like sequences in grossly inhomogeneous B_0 and B_1 fields and application to NMR well logging, J. Magn. Res. 143 (2000) 120–135.

[13] M.D. Hürlimann, Diffusion and relaxation effects in general stray field NMR experiments, J. Magn. Res. 148 (2001) 367–378.

[14] Y.-Q. Song, Categories of coherence pathways for the CPMG sequence, J. Magn. Res. 157 (2002) 82–91.

[15] Y. Zur, An algorithm to calculate the NMR signal of a multi spin-echo sequence with relaxation and spin-diffusion, J. Magn. Res. 171 (2004) 97–106.

[16] K.-J. Dunn, Enhanced transverse relaxation in porous media due to internal field gradients, J. Magn. Res. 156 (2002) 171–180.

[17] C.S. Johnson Jr., Q. He, Electrophoretic nuclear magnetic resonance, in: J.S. Waugh (Ed.), Advances in Magnetic Resonance 13, Academic Press, London, 1989, pp. 131–159.

[18] A. Caprihan, E. Fukushima, Flow measurements by NMR, Phys. Rep. 198 (1990) 195–235.

[19] E. Fukushima, S.B.W. Roeder, Experimental Pulse NMR: A Nuts and Bolts Approach, Addison-Wesley, Reading, Massachusetts, 1981.

[20] S.-W. Lo, G.J. Hirasaki,W.V. House, R. Kobayashi, Mixing rules and correlations of NMR relaxation time with viscosity, diffusivity, and gas/oil ratio of methane/hydrocarbon mixtures, SPE paper 77264, SPE J. 7 (2002) 24–34.

[21] M. Winkler, J.J. Freeman, M. Appel, The limits of fluid property correlations used in NMR well-logging: an experimental study of reservoir fluids at reservoir conditions, Petrophysics 46 (2005) 104–112.

[22] H. Torrey, Bloch equations with diffusion terms, Phys. Rev. 104 (1956) 563–565.

[23] R.M. Weiskoff, C.S. Zuo, J.L. Boxerman, B.R. Rosen, Microscopic susceptibility variation and transverse relaxation: theory and experiment, Magn. Res. Med. 31 (1994) 601–609.

[24] L.M. Schwartz, J.R. Banavar, Transport properties of disordered continuum systems, Phys. Rev. B 39 (1989) 11965–11970.

[25] D.J. Wilkinson, D.L. Johnson, L.M. Schwartz, Nuclear magnetic relaxation in porous media: the role of the mean lifetime τ (ρ,D), Phys. Rev. B 44 (1991) 4960–4973.

[26] D.J. Bergman, K.-J. Dunn, L.M. Schwartz, P.P. Mitra, Self-diffusion in a periodic porous medium: a comparison of different approaches, Phys. Rev. E 51 (1995) 3393–3400.

[27] H. Gudbjartsson, S. Patz, NMR diffusion simulation based on conditional random walk, IEEE Trans. Med. Imag. 14 (1995) 636–642.

[28] C.P. Slichter, Principles of Magnetic Resonance, Springer, New York, 1992.

[29] P. Sen, A. André, S. Axelrod, Spin echoes of nuclear magnetization diffusing in a constant magnetic field gradient and in a restricted geometry, J. Chem. Phys. 111 (1999) 6548–6555.

[30] K.S. Mendelson, Continuum and random-walk models of magnetic relaxation in porous media, Phys. Rev. B 47 (1993) 1081–1083.

[31] W.E. Kenyon, Petrophysical principles of applications of NMR logging, Log Analyst 38 (1997) 21–43.

[32] E. Toumelin, C. Torres-Verdín, B. Sun, K.-J. Dunn, Limits of 2D NMR interpretation techniques to quantify pore size, wettability, and fluid type: a numerical sensitivity study, SPE J. 11 (2006) 354–363.

[33] E. Toumelin, C. Torres-Verdín, S. Devarajan, B. Sun, An integrated pore-scale approach for the simulation of grain

morphology, wettability, and saturation-history effects on electrical resistivity and NMR measurements of saturated rocks, Paper presented at the 2006 International Symposium of the Society of Core Analysts, Trondheim, Norway, September 12–16.

[34] G. Hirasaki, Wettability: fundamentals and surface forces, SPE Formation Eval. 6 (1991) 217–226.

[35] A.R. Kovscek, H. Wong, C.J. Radke, A pore-level scenario for the development of mixed wettability in oil reservoirs, AIChE J. 39 (1993) 1072–1085.